



**HAL**  
open science

# **Borna Disease Virus 1 Phosphoprotein Forms a Tetramer and Interacts with Host Factors Involved in DNA Double-Strand Break Repair and mRNA Processing**

Nicolas Tarbouriech, Florian Chenavier, Junna Kawasaki, Kamel Bachiri, Jean-Marie Bourhis, Pierre Legrand, Lily Freslon, Estelle Laurent, Elsa Suberbielle, Rob Ruigrok, et al.

► **To cite this version:**

Nicolas Tarbouriech, Florian Chenavier, Junna Kawasaki, Kamel Bachiri, Jean-Marie Bourhis, et al.. Borna Disease Virus 1 Phosphoprotein Forms a Tetramer and Interacts with Host Factors Involved in DNA Double-Strand Break Repair and mRNA Processing. *Viruses*, 2022, 14 (11), pp.2358. 10.3390/v14112358 . hal-03834032

**HAL Id: hal-03834032**

**<https://hal.science/hal-03834032v1>**










Submitted on 28 Oct 2022

**HAL** is a multi-disciplinary open access archive for the deposit and dissemination of scientific research documents, whether they are published or not. The documents may come from teaching and research institutions in France or abroad, or from public or private research centers.

L'archive ouverte pluridisciplinaire **HAL**, est destinée au dépôt et à la diffusion de documents scientifiques de niveau recherche, publiés ou non, émanant des établissements d'enseignement et de recherche français ou étrangers, des laboratoires publics ou privés.

## Article

# Borna Disease Virus 1 Phosphoprotein forms a Tetramer and Interacts with Host Factors Involved in DNA Double-Strand Break Repair and mRNA Processing

Nicolas Tarbouriech <sup>1</sup>, Florian Chenavier <sup>1,†</sup>, Junna Kawasaki <sup>2,3,†</sup>, Kamel Bachiri <sup>4,†</sup>, Jean-Marie Bourhis <sup>1</sup>, Pierre Legrand <sup>5</sup>, Lily L. Freslon <sup>1</sup>, Estelle M. N. Laurent <sup>4</sup>, Elsa Suberbielle <sup>6</sup>, Rob W. H. Ruigrok <sup>1</sup>, Keizo Tomonaga <sup>2,3,7</sup>, Daniel Gonzalez-Dunia <sup>6</sup>, Masayuki Horie <sup>8,9</sup>, Etienne Coyaud <sup>4</sup> and Thibaut Crépin <sup>1,\*</sup>

- <sup>1</sup> Institut de Biologie Structurale (IBS), CEA, CNRS, Université Grenoble Alpes, 38058 Grenoble, France  
<sup>2</sup> Laboratory of RNA Viruses, Department of Virus Research, Institute for Life and Medical Sciences, Kyoto University, Kyoto 606-8507, Japan  
<sup>3</sup> Laboratory of RNA Viruses, Department of Mammalian Regulatory Network, Graduate School of Biostudies, Kyoto University, Kyoto 606-8507, Japan  
<sup>4</sup> Department of Biology, Univ. Lille, Inserm, CHU Lille, U1192—Protéomique Réponse Inflammatoire Spectrométrie de Masse—PRISM, 59000 Lille, France  
<sup>5</sup> Synchrotron SOLEIL, L'Orme des Merisiers, 91192 Gif-sur-Yvette, France  
<sup>6</sup> Institut Toulousain des Maladies Infectieuses et Inflammatoires (Infinity), Université de Toulouse, Inserm, CNRS, UPS, 31024 Toulouse, France  
<sup>7</sup> Department of Molecular Virology, Graduate School of Medicine, Kyoto University, Kyoto 606-8507, Japan  
<sup>8</sup> Laboratory of Veterinary Microbiology, Graduate School of Veterinary Science, Osaka Metropolitan University, Izumisano 598-8531, Japan  
<sup>9</sup> Osaka International Research Center for Infectious Diseases, Osaka Metropolitan University, Izumisano 598-8531, Japan  
\* Correspondence: thibaut.crepin@ibs.fr  
† These authors contributed equally to this work.



**Citation:** Tarbouriech, N.; Chenavier, F.; Kawasaki, J.; Bachiri, K.; Bourhis, J.-M.; Legrand, P.; Freslon, L.L.; Laurent, E.M.N.; Suberbielle, E.; Ruigrok, R.W.H.; et al. Borna Disease Virus 1 Phosphoprotein forms a Tetramer and Interacts with Host Factors Involved in DNA Double-Strand Break Repair and mRNA Processing. *Viruses* **2022**, *14*, 2358. <https://doi.org/10.3390/v14112358>

Academic Editors: Kore Schlottau and Dennis Rubbenstroth

Received: 23 September 2022

Accepted: 24 October 2022

Published: 26 October 2022

**Publisher's Note:** MDPI stays neutral with regard to jurisdictional claims in published maps and institutional affiliations.



**Copyright:** © 2022 by the authors. Licensee MDPI, Basel, Switzerland. This article is an open access article distributed under the terms and conditions of the Creative Commons Attribution (CC BY) license (<https://creativecommons.org/licenses/by/4.0/>).

**Abstract:** Determining the structural organisation of viral replication complexes and unravelling the impact of infection on cellular homeostasis represent important challenges in virology. This may prove particularly useful when confronted with viruses that pose a significant threat to human health, that appear unique within their family, or for which knowledge is scarce. Among *Mononegavirales*, bornaviruses (family *Bornaviridae*) stand out due to their compact genomes and their nuclear localisation for replication. The recent recognition of the zoonotic potential of several orthobornaviruses has sparked a surge of interest in improving our knowledge on this viral family. In this work, we provide a complete analysis of the structural organisation of Borna disease virus 1 (BoDV-1) phosphoprotein (P), an important cofactor for polymerase activity. Using X-ray diffraction and diffraction experiments, we revealed that BoDV-1 P adopts a long coiled-coil  $\alpha$ -helical structure split into two parts by an original  $\beta$ -strand twist motif, which is highly conserved across the members of whole *Orthobornavirus* genus and may regulate viral replication. In parallel, we used BioID to determine the proximal interactome of P in living cells. We confirmed previously known interactors and identified novel proteins linked to several biological processes such as DNA repair or mRNA metabolism. Altogether, our study provides important structure/function cues, which may improve our understanding of BoDV-1 pathogenesis.

**Keywords:** *Bornaviridae*; phosphoprotein; structure; interactomics

## 1. Introduction

Nonsegmented negative-strand RNA viruses (or *Mononegavirales*) are a class of viruses that infect plants and animals, with many of them causing significant diseases or even death in humans. These enveloped viruses share common strategies in viral replication

and/or gene expression [1]. Their genome, encapsulated by the nucleoprotein (N), is the biologically active template for both transcription and replication by the polymerase complex [2] resulting from the association of the viral RNA-dependent RNA polymerase (RdRp or L) with its essential cofactor, phosphoprotein (P). P is a highly versatile protein involved in numerous functions, with a high degree of structural flexibility. Through its modular architecture consisting of long disordered regions that alternate with structured domains, P interacts with the main proteins of the viral RNA synthesis machine. It self-associates in oligomers through a central oligomerisation domain ( $P_{OD}$ ) [3–12] and bridges the RdRp [13–19] and the nucleocapsid [20]. It also chaperones N to maintain it in an RNA-free form needed for replication [21–28]. In addition, P is an essential actor of viral replication by recruiting a plethora of cellular partners with proviral activities [10,29–40]. The disordered regions of P seem to be of primary importance for these additional functions.

Bornaviruses (family *Bornaviridae*) occupy a special place within *Mononegavirales*. They infect the widest range of species of the animal kingdom, ranging from fishes to mammals [41–43]. While most mononegaviruses mainly perform cytoplasmic replication, bornaviruses replicate in the nucleus, where they assemble viral factories [44] designated as “viral Speckles Of Transcripts” (vSPOTs). It has been recently shown that some mammalian orthobornaviruses (*e.g.*, Borna disease virus 1 (BoDV-1) and variegated squirrel bornavirus 1 (VSBV-1)) can infect humans, predominantly affecting neuronal tissues and causing fatal encephalitis [45–47]. The genome of bornaviruses consists of approximately 8900 nucleotides and represents the smallest known genome amongst *Mononegavirales*. BoDV-1 vSPOTs formed by P protein-driven liquid–liquid phase separation [48], are present in the nucleus, in close interaction with the chromatin, where they dock on neuronal DNA double-strand breaks (DSBs), thereby affecting neuronal epigenetics and activity [49]. In particular, both N and P seem to modulate epigenetic signalling in neurons [50,51].

BoDV-1 replicative machinery, a complex between the RdRp (L) and P, produces different mRNAs from the genome via polar sequential transcription, encoding for a total of six viral proteins. Except for the RNA-free N and the matrix protein [52,53], nothing is known concerning the structure of these viral proteins. Here, we used X-ray diffraction and diffraction experiments to provide a complete structural analysis of BoDV-1 P. We observed that P possesses a modular architecture, consisting of a central oligomerisation domain ( $P_{OD}$ ) surrounded by two disordered regions, similar to other *Mononegavirales* Ps. We also showed that BoDV-1  $P_{OD}$  has the most elongated multimerisation domain of all mononegaviruses, with one monomer composed of two consecutive  $\alpha$ -helices linked by a short three-amino acid stretch, making a 140 Å long coiled-coil  $\alpha$ -helical structure split into two parts by a  $\beta$ -strand twist motif. This particular motif appears to be important for viral replication and is highly conserved across the members of the whole *Orthobornavirus* genus. Moreover, we determined the BoDV-1 P proximal interactome in human cells, confirming previous interactors and identifying novel proteins linked to DNA breaks and mRNA metabolism. Interestingly, the strong overlap between the proximal interactomes in living cells of N- and C-terminal biotin ligase (BirA<sub>R118G</sub>, or BirA\*)-tagged BoDV-1 P data in living cell suggests that this structure is highly flexible at the  $\beta$ -strand twist motif and/or that the disordered domains confer enough freedom of movement to the BirA\* moiety to biotinylate a highly similar protein environment regardless of its position in the primary protein sequence. Altogether, our results provide important advances in our understanding of the structural organisation of BoDV-1 P protein and strongly support the relevance of our structural model in a living cellular context.

## 2. Materials and Methods

### 2.1. Cloning and Plasmid Preparation

The bacterial expression-optimised DNA coding sequence of Borna disease virus 1 (BoDV-1) P was purchased from GeneArt (ThermoFischer Scientific, Regensburg, Germany). Primers were designed for the amplification of the different constructs of BoDV-1 (residues 1 to 201 and 65 to 172), munia bornavirus 1 (MuBV-1; residues 65 to 172), and Gaboon viper

virus 1 (GaVV-1; residues 67 to 178). Each DNA fragment was cloned into pETM11 bacterial expression vector (EMBL) using 5' end *Nco1* and 3' end *Xho1* restriction sites introduced by PCR amplification. All constructs were expressed as N-terminally TEV-removable His-tagged proteins. Sequencing verifications were performed by Eurofins Genomics.

## 2.2. Protein Expression and Protein Purification

Plasmids with the corresponding constructs were transformed into *Escherichia coli* BL21 RIL (DE3) cells (Life Technologies, Thermo Fischer Scientific, Villebon-sur-Yvette, France). LB cultures were induced for 12 h with 0.3 mM isopropyl- $\beta$ -D-thiogalactopyranoside (IPTG) at 18 °C, collected by centrifugation, and stored at  $-80$  °C. Briefly, Bacterial pellets were resuspended in 50 mM Tris-HCl (pH 7.5), 500 mM NaCl, 1 mM  $\beta$ -mercaptoethanol ( $\beta$ -ME), and cOmplete™ ethylenediaminetetraacetic acid (EDTA)-free protease inhibitor cocktail (Roche, Meylan, France). After lysis by sonication and centrifugation, the supernatant was complemented with 15 mM imidazole and the recombinant proteins were purified by nickel affinity chromatography (resin Ni-NTA; Qiagen, Courtabœuf, France). Based on SDS-PAGE analysis, fractions of interest were pooled together before the addition of 1% tobacco etch virus (TEV) protease and dialysed overnight in 20 mM HEPES (pH 7.5), 200 mM NaCl, and 1 mM  $\beta$ -ME. A second nickel affinity chromatography was performed to remove both the uncleaved protein of interest and TEV protease before the size-exclusion chromatography (SEC). The flow-through was concentrated by centrifugation (Millipore-Amicon Ultra centrifugal filters 10 K) and injected into a HiLoad™ S200 16/600 column (Cytiva, Velizy-Villacoublay, France) with a NGC system (Bio-Rad, Marnes-La-Coquette, France). All proteins were in the same final buffer composed of 20 mM HEPES (pH 7.5), 150 mM NaCl, and 1mM  $\beta$ -ME.

## 2.3. Crystallisation and X-ray Structure Determination

Crystallisation experiments were initiated using the HTX platform (EMBL, Grenoble, France) before a final manual screening to obtain single crystals. BoDV-1  $P_{OD}$  crystals were obtained from a  $10 \text{ mg}\cdot\text{mL}^{-1}$  protein solution using a precipitant composed of 100 mM HEPES (pH 7.5), 14–18% polyethylene glycol (PEG) 8K, and 200 mM  $\text{CaCl}_2$ . MuBV-1  $P_{OD}$  crystals were obtained from a  $4 \text{ mg}\cdot\text{mL}^{-1}$  protein solution using a precipitant composed of 15–18% PEG 3350, 150 mM  $\text{Mg}(\text{NO}_3)_2$ , and 10 mM phenol. GaVV-1  $P_{OD}$  crystals were obtained from a  $5 \text{ mg}\cdot\text{mL}^{-1}$  protein solution using a precipitant composed of 100 mM HEPES (pH 7.5), 18–22% PEG 3350, and 200 mM NaSCN. Crystals were cryo-protected in their mother liquor solution containing 20% glycerol, mounted on cryoloops (Hampton Research, Aliso Viejo, CA, USA), and frozen in liquid nitrogen.

BoDV-1  $P_{OD}$  diffraction experiments were undertaken on ID-29 at the European Synchrotron Radiation Facility (ESRF, Grenoble, France). Data were collected using a Dectris Pilatus 6M detector. Indexing and integration were performed using the XDS program suite [54,55]. Thereafter, data were processed using STARANISO [56], as implemented in autoPROC [57], which applies non-elliptical anisotropic limits based on a locally averaged mean  $I/\sigma(I)$  cut-off, performs a Bayesian estimation of structure amplitudes, and applies an anisotropic correction to the data. Detailed crystallographic statistics are provided in Table S1. Molecular replacement solutions were obtained with Phaser [58] using the measles virus  $P_{OD}$  structure [6]. The initial solution was then used through repeated cycles of autobuilding using Autobuild [59] within the Phenix suite [60]. The final building phase used both manual model building with COOT [61], together with Autobuild cycles and ArpWarp [62,63]. Refinement of the model was carried out using Refmac5 [64].

MuBV-1  $P_{OD}$  diffraction experiments were undertaken on PROXIMA-1 at the SOLEIL Synchrotron (Saint-Aubin, France). Data were collected using a Dectris Eiger-X 16M detector. Indexing and integration were performed using the XDS program suite. Molecular replacement solutions were obtained with Phaser using the BoDV-1  $P_{OD}$  tetrameric structure separated into two ensembles: one containing residues 86 to 125 and the other

containing residues 127 to 166. The final building phase used both a manual model building with COOT and refinement of the model using Refmac5.

GaVV-1 POD diffraction experiments were undertaken on PROXIMA-1 for the native dataset and on PROXIMA-2A for the Se-SAD dataset at the SOLEIL Synchrotron. PROXIMA-2A is equipped with a Dectris Eiger-X 9M detector. Indexing and integration were performed using the XDS program suite. Heavy atoms sites were determined using the SHELX suite [65], their positions were refined using PHASER in EP mode, and the phases were improved using PARROT [66] for density modification. The resulting electron density allowed the positioning of an AlphaFold2 [67] model, which was improved and refined against the native dataset with COOT and Refmac5.

The figures were drawn using PyMOL [68].

#### 2.4. Small-Angle X-ray Scattering (SAXS) Analysis

All datasets were collected on the SWING beamline at the SOLEIL synchrotron. The collection parameters are listed in Table S2. The samples were loaded onto a Superdex<sup>TM</sup> 200 increase 5/150 GL (Cytiva) SEC column and SAXS measurements were performed throughout elution, operating at 20 °C with a flow rate of 0.3 mL·min<sup>-1</sup> and a mobile phase containing 20 mM HEPES (pH 7.5), 150 mM NaCl, and 5 mM β-ME. The data were integrated and subtracted with Foxtrot [69], providing the first estimation of I(0) and R<sub>g</sub> for each frame of the SEC profile. This allowed the identification along the elution peak of the frames with constant R<sub>g</sub> values. The corresponding frames were merged into a final scatter curve used for further analysis. Final R<sub>g</sub> values were determined using ATSAS [70] and RAW [71]. D<sub>max</sub> values were determined using GNOM [72] in the ATSAS suite and compared to the values obtained with BIFT [73] implemented in RAW. Molecular weights of the proteins were estimated by using the Q<sub>r</sub> ratio derived from the invariant volume of correlation [74].

#### 2.5. Ab Initio Molecular Shape Analysis of P<sub>OD</sub>

*Ab initio* shape analyses were performed using DAMMIF [75] from the ATSAS package. Twenty independent DAMMIF calculations were performed both with and without four-fold (P<sub>4</sub>) symmetry. In each case, to create the most probable molecular shape, an average shape was determined with DAMAVER [76], with and without P<sub>4</sub> symmetry. The filtered models were then reprocessed against the experimental data using DAMMIN [77].

#### 2.6. Full Atom Modelling of BoDV-1 P<sub>FULL</sub>

An initial pool of 10,000 random conformation models of BoDV P<sub>FULL</sub> was generated using the Ensemble Optimisation Method (EOM 2.1 [78]). The models generated for the disordered N-terminal (residues 1 to 71) and C-terminal segments (residues 167 to 201) were attached to the P<sub>OD</sub> X-ray structure. As the disordered parts generated by EOM are C<sub>α</sub>, we used an in-house procedure to obtain the full atom structures of the pool. First, PD2 ca2main [79] was used to reconstruct the backbone, followed by SCWRL4 [80] to add the side chains. This pool was then used to select a final ensemble with the EOM algorithm based on the experimental scattering curve. This process was repeated three times.

#### 2.7. Minireplicon Assays

Minireplicon assays were conducted as described previously [81]. Briefly, 293T cells seeded onto 48-well plates were transfected with 50 ng of minigenome plasmid containing *Gaussia* luciferase as a reporter gene [82], 50 ng of pCAGGS-N, 5 ng of pCAGGS-P (or point-mutated P), and 50 ng of pCAGGS-L using TransIT293 (Mirus) according to the manufacturer's instructions. The culture supernatants were collected at 72 h post transfection and subjected to luciferase assay using a Bioluminescence Assay Kit (New England BioLabs, Evry, France) according to the manufacturer's instructions. The assays were performed in technical duplicates for each experiment.



### 2.8. Determination of Proximal Host–Viral Protein Interactions in Living Cells (BioID)

These experiments were performed as in [83]. Briefly, Flp-In™ T-REX™ HEK293 cells (Life Technologies) cells were co-transfected with pOG44 (encoding the Flp recombinase) and pcDNA5 FRT/TO FlagBirA\*<sup>-</sup> or BirA\*Flag P<sub>FULL</sub> (N- and C-ter tag, respectively) of BoDV-1. Cells were selected with Hygromycin B to generate new stable tetracycline-inducible cell lines expressing single copies of N- and C-terminal tagged P<sub>FULL</sub>-BirA\* fusion proteins. Cultures were expanded to ~100 million cells per sample, before being placed into a medium of 1 µg·mL<sup>-1</sup> tetracycline to induce bait protein expression, along with 50 µM biotin. After 24 h, induction cells were collected, washed twice with PBS, spun down, and stored at –80 °C. Each pellet was resuspended in a 5 mL of modified RIPA buffer (50 mM Tris-HCl (pH 7.5), 150 mM NaCl, 1 mM EDTA, 1 mM EGTA, 1% Triton X-100, 0.1% SDS, 1:500 protease inhibitor cocktail (Sigma-Aldrich, Saint-Quentin Fallavier, France), and 1:1000 Turbonuclease (BPS Bioscience, Nanterre, France)), incubated for one hour on an end-over-end rotator at 4 °C, sonicated until no visible aggregates remained, and centrifuged at 45,000 × g for 20 min. Cleared supernatants containing all compartment solubilized proteins were transferred to new tubes and incubated with 30 µL of packed and pre-equilibrated streptavidin resin (Ultralink, Pierce, Thermo Fischer Scientific, Villebon-sur-Yvette, France; 2 h under rotation at 4 °C) to capture biotinylated species. Beads were pelleted (300 g, 1 min) and washed six times with 50 mM ammonium bicarbonate (AB). Trypsin (1 µg) was added to each 200 µL sample to digest on beads (overnight at 37 °C). Tryptic peptides were collected in the supernatant, lyophilized, and desalted on C18 ziptips. One-quarter of each sample was analysed by nLC MS-MS (Easy1000 in line with a Thermo Q-Exactive; see Supplemental Methods). The MS raw files were then analysed using MaxQuant (version 1.5.8.3) against the UniProt Reference database to generate the protein identification list with a 1% FDR. High confidence proximal interactors were defined using Perseus (version 1.6.15.0) with the following filters for each given ID: peptides detected in 3/3 bait protein runs; an average Log<sub>2</sub> LFQ abundance against average top 3/20 control over 1; and a corresponding q-value < 0.01 (Table S3).

## 3. Results

### 3.1. X-ray Structure of the Oligomerisation Domain of BoDV-1 Phosphoprotein

With *Mononegavirales* Ps being known as multimodular nonglobular molecules, we first performed a bioinformatic analysis of the BoDV-1 P amino acid sequence using 16 web servers, all of them predicting the location of disordered regions and secondary structure elements. We then combined all of the results in a single representation (D-score; Figure 1a). On this graph, residues with a D-score <0.50 were assigned as disordered, while residues with a D-score >0.5 were assigned as structured. We observed that BoDV-1 P presented an organisation similar to other *Mononegavirales* Ps, with central folded domains flanked by N- and C-terminal disordered regions. Structure prediction using AlphaFold2 is compatible with the D-score analysis (Figure S11). Based on this prediction, two constructs were designed (Figure 1b): the full-length P (P<sub>FULL</sub>) and the central domain (from residue 65 to 172) that we hypothesized to be the oligomerisation domain (P<sub>OD</sub>), even if its size represented nearly half of the protein length and was much longer than P<sub>OD</sub> from other viruses.

BoDV-1 P<sub>OD</sub> crystals (fine plates growing in urchins) were obtained in PEG 8000, only in the presence of calcium chloride. Crystals belonged to space group *P42<sub>1</sub>2*, with cell parameters *a* = *b* = 35 Å and *c* = 166 Å. The analysis of the asymmetric unit indicated that it could only contain a single-amino acid chain (Matthew coefficient of 2.1 Å<sup>3</sup>·Da<sup>-1</sup> with a solvent content of 42% for a 108 amino acid-long chain), meaning that it was likely to contain a single narrow elongated molecule. This informed our choice to use a single coiled-coil chain of the measles virus tetrameric P<sub>OD</sub> [6] as a starting model to solve the structure by molecular replacement. An initial solution was obtained from Phaser [58] and improved using Autobuild [59], before being classically built and refined. The final structure is shown in Figure 2a.

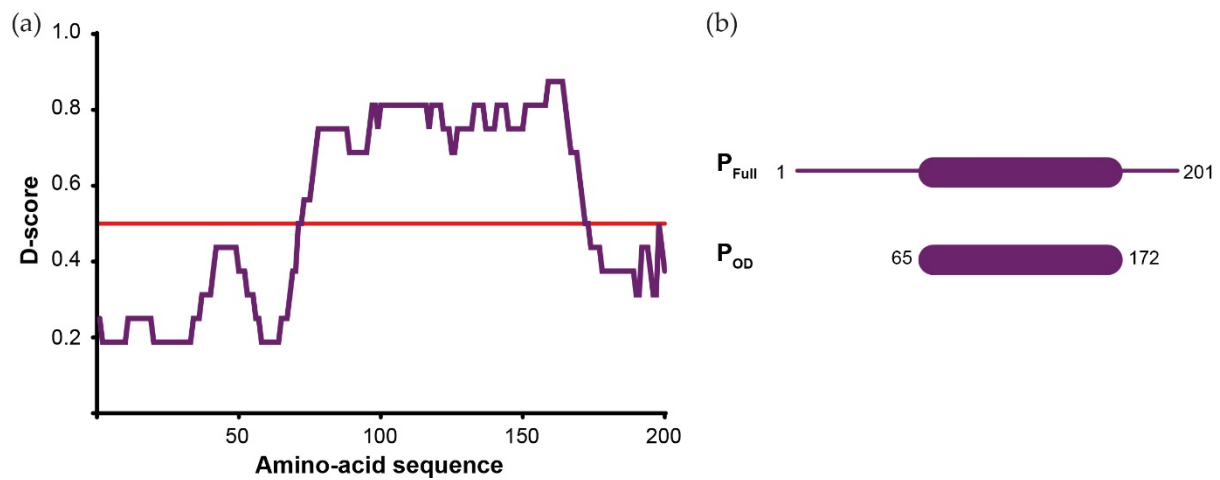


**Figure 1.** Predicted architecture of BoDV-1 phosphoprotein. (a) D-score (score for disorder as a function of residue) of BoDV-1 P. The prediction was based on 16 predictor web servers and the D-score was calculated by adding the values for each residue and dividing by the number of used algorithms. We arbitrarily defined a threshold level at 0.50. Residues with a D-score <0.50 were assigned as disordered [84]. (b) Scheme of the BoDV-1 P constructs designed for this work based on the bioinformatics analysis.

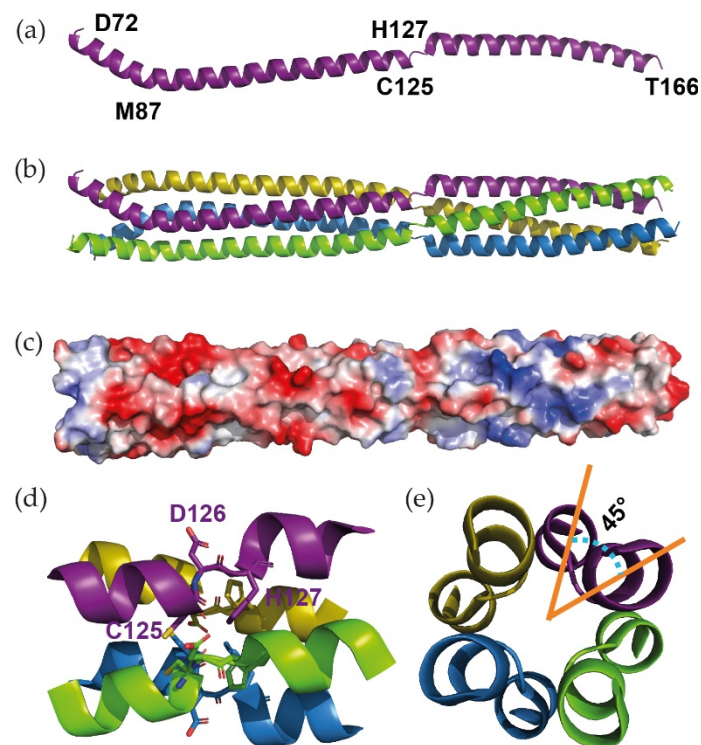


**Figure 2.** X-ray structure of BoDV-1  $P_{OD}$ . (a) Structure of BoDV-1 monomeric  $P_{OD}$  as obtained in the asymmetric unit. (b) Structure of the tetrameric  $P_{OD}$  after applying the inherent symmetry operations of the tetragonal space group. The four parallel monomers are coloured in purple, yellow, blue, and green, respectively. (c) Electrostatic surface potential of  $P_{OD}$ . The potential scale ranges from  $-5$  kT/e (red) to  $5$  kT/e (blue); the orientation is as in (b). (d) Detail of the  $\beta$ -strand twist motif that separates the two  $\alpha$ -helical coiled-coils. (e) Orthogonal view of the  $\beta$ -strand twist motif as shown in (d), showing the  $45^\circ$  rotation of the helical axis around the super helical axis.

The monomeric  $P_{OD}$  is composed of two consecutive aligned  $\alpha$ -helices (from residue E73 to Q123 and S128 to A164, respectively) linked by a short stretch of three residues,

making a  $\approx 140$  Å long molecule. As most *Mononegavirales* P assemble in oligomers through their central domain, we analysed  $P_{OD}$  by SAXS (Table S2) in order to compare its behaviour in the crystal and in solution. With a  $D_{max}$  of  $170 \pm 9$  Å, it confirmed one dimension of the protein. Furthermore, the volume of correlation ( $V_c$ ) determination method [74] estimated a  $M_w$  of 40 kDa, corresponding to a tetramer (discussed later in Section 3.3). A tetrameric  $P_{OD}$  could then be reconstituted by applying the inherent 4-fold symmetry of this tetragonal space group (Figure 2b). It was then composed of two  $\alpha$ -helical coiled-coils with all the monomers being parallel, with a break centred at position 126 in the middle of the whole structure (Figure 2d and Figure S9). Considering the electrostatic surface of the domain, the break seemed to separate the N-terminal acidic region from the C-terminal more neutral region (Figure 2c). A careful analysis of the Crick parameters [85,86] using CCCP [87] and TWISTER [88] demonstrated a decrease in the helical and superhelical radius together with an increase in the rise per residue and a decrease in the periodicity. In addition, the Ramachandran plot showed that residue D126 fell into the  $\beta$ -area, whereas neighbouring residues (C125 and H127) were in intermediate positions, between the  $\alpha$ - and the  $\beta$ -areas (Figure S1a). Altogether, our data point towards the formation of a  $\beta$ -strand twist motif within the helices, as described for trimeric oligomerisation domains [89]. As opposed to the trimers, the tetrameric motif of  $P_{OD}$  identified herein did not form regular  $\beta$ -sheet main chain hydrogen bonds, and the shift in the helical axis was limited to  $45^\circ$  (Figure 2e) instead of the  $120^\circ$  observed in trimers.

### 3.2. The $\beta$ -Strand Twist of BoDV-1 P Is Important for Viral Replication

In order to assess the involvement of the  $\beta$ -strand twist motif in BoDV-1 replication, we performed minireplicon assays using a series of P mutants, each one bearing a single amino acid substitution at the twist or in its proximal regions (from position 124 to 129). 293T cells were then transfected with a minigenome plasmid containing the *Gaussia luciferase* as a reporter gene, together with plasmids encoding for N, L, and different versions of P. The *Gaussia luciferase* activity levels were then measured (Figure 3a). Correct expression of each P mutant was confirmed by western blotting (Figure 3b). Interestingly, substitutions by alanine of R124 and D129, two proximal residues of the motif, did not affect the polymerase activity. Rather, the activity was abolished or markedly reduced by mutating C125, D126, or H127. Note that the quantity of protein for this mutant, as well as for the second mutant tested for this position (*i.e.*, C125D), appeared strongly reduced in the western blot analysis. Altogether, these results suggest that the  $\beta$ -strand twist motif is important for BoDV-1 replication, notably concerning D126 and H127 residues, whereas C125 would have an effect on the stability and/or the folding of P. Cysteine residues are known to form disulfide bridges and stabilise the structuration of secreted proteins. Surprisingly for a nuclear protein, such a disulfide bridge has been previously proposed at position 125 of BoDV-1 P [90]. Our experimental conditions did not allow us to detect them, especially in the crystal structure. However, compared to D126, which is strictly conserved (Figure 4j and Figure S8), the amino acid in position 125 is a cysteine only in mammalian 1 orthobornaviruses (*i.e.*, BoDV-1 and -2).



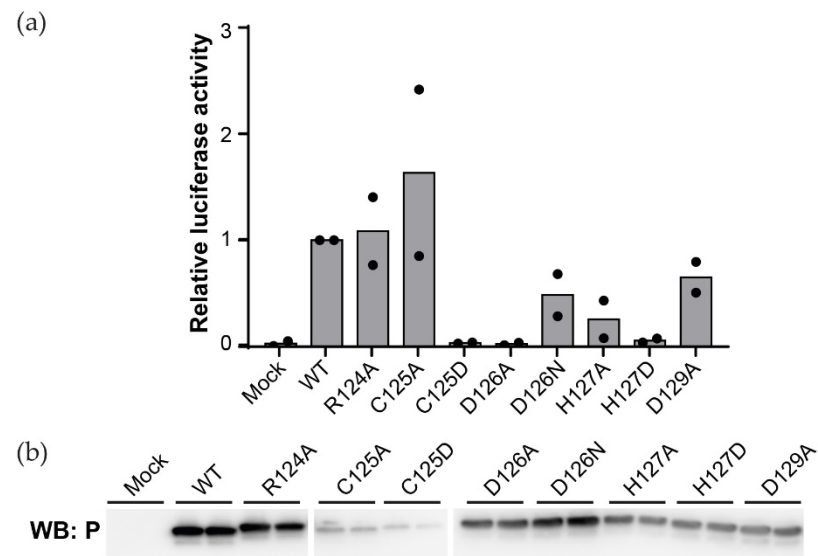


**Figure 3.** Mutations within the  $\beta$ -strand twist motif of BoDV-1 P modulates viral replication. (a) Minireplicon assay using a series of P mutants. The relative luciferase activities are shown as the ratios relative to wild-type P transfected cells (WT). The indicated BoDV-1 P mutants were used as helper plasmids. The dots show mean values (biological replicates;  $n = 2$ ). (b) Detection of BoDV-1 P mutants by western blotting. The whole western blot is shown in Figure S7.

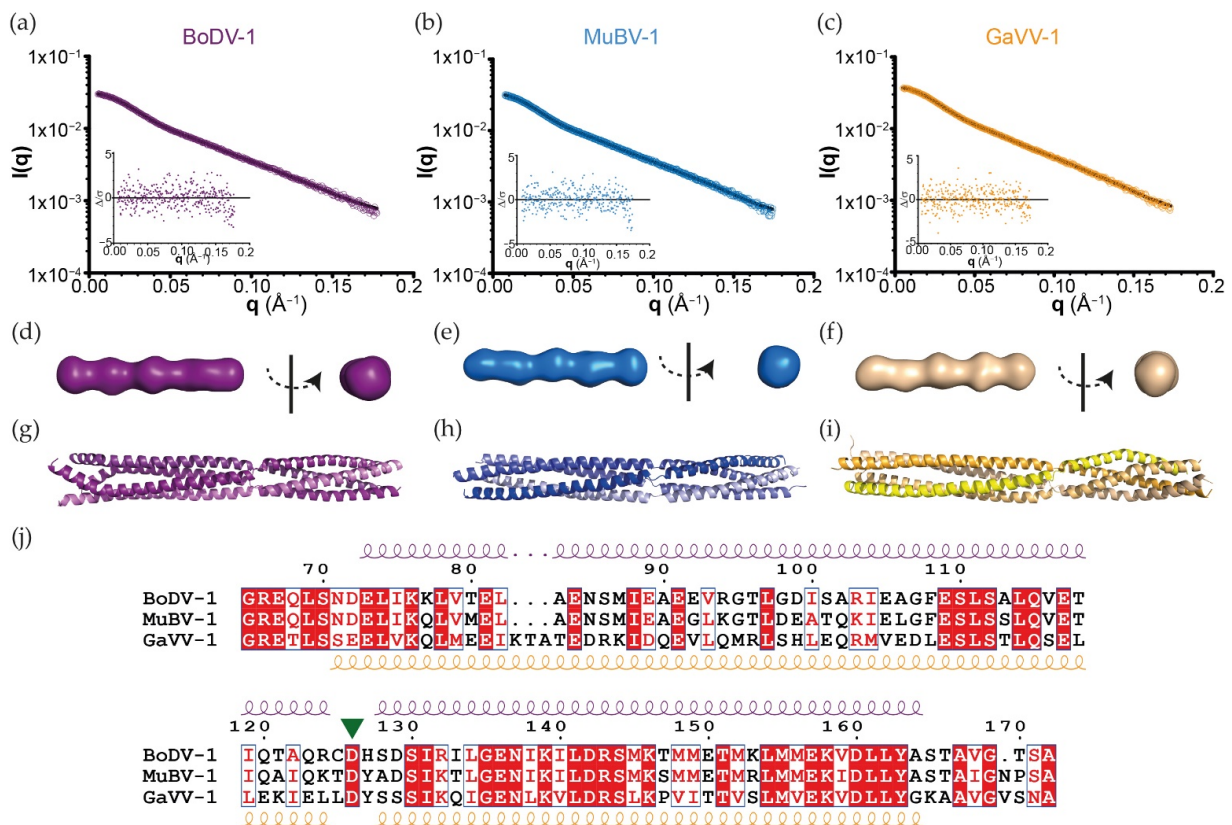


**Figure 4.** Structural analysis of orthobornaviral P<sub>OD</sub>. Experimental SAXS diffraction curves (with residuals (small plots)) of (a) BoDV-1, (b) MuBV-1, and (c) GaVV-1 P<sub>OD</sub> overlaid with the averaged SAXS curves (black) resulting from the *ab initio* models shown in panels d–f. Low-resolution envelopes of (d) BoDV-1, (e) MuBV-1, and (f) GaVV-1 P<sub>OD</sub> based on the *ab initio* modelling from the SAXS data. X-ray structure of (g) BoDV-1, (h) MuBV-1, and (i) GaVV-1 P<sub>OD</sub> with the same orientation (*i.e.*, N-terminal on the left). The SAXS envelopes (d–f) and the X-ray structures (g–i) are not at the same s-

cale. Figure S4 presents the dockings of the X-ray structures in the SAXS envelopes. (j) Sequence alignment of the corresponding  $P_{OD}$  with the secondary structures of BoDV-1 and GaVV-1, shown above and below the sequence alignment, respectively. Residues in a solid red background are identical between the three sequences. The green triangle indicates the position of the conserved aspartate residue within the  $\beta$ -strand twist motif.

### 3.3. The $\beta$ -Strand Twist Motif Is Conserved in Orthobornavirus $P_{OD}$

The comparison with tetrameric oligomerisation domains of P from other *Mononegavirales* (metapneumovirus, parainfluenza 5, measles, mumps, Nipah and murine respirovirus) showed that BoDV-1  $P_{OD}$  was indeed the longest (the size of one monomer in the corresponding X-ray structures is 141, 100, and 93 Å long for BoDV-1, murine respirovirus, and measles  $P_{OD}$ , respectively). Above all, it is the only one with such a  $\beta$ -strand twist-like motif that breaks the continuity of its  $\alpha$ -helical coiled-coil organisation. We therefore investigated its conservation in other members of the *Bornaviridae* family. Several  $P_{OD}$  were cloned, expressed, and purified. Crystals were obtained for the  $P_{OD}$  of munia bornavirus 1 (MuBV-1; 77% sequence identity with BoDV-1) and Gaboon viper virus 1 (GaVV-1; 41 and 43% sequence identity with BoDV-1 and MuBV-1, respectively). The complete SEC-SAXS and X-ray analysis of the three  $P_{OD}$  were performed (Figure 4).

In solution, the three  $P_{OD}$  presented the same behaviour. They were all eluted as a single straight symmetric peak from the SEC-SAXS column, without any aggregate signal. Using the Vc determination on the diffusion data, the MW were estimated between 40 and 45 kDa, 12–16% lower than the theoretical values (Table S2 and Figures S2–S4), all corresponding to tetramers. The Guinier transforms measured a hydrodynamic radius ( $R_g$ ) between 44 and 46 Å and GNOM produced the pair distribution functions that fit with  $D_{max}$  between 169 and 178 Å. Independently to the X-ray crystallography analysis, *ab initio* modelling was performed using twenty DAMMIF models averaged by DAMAVER. Averaged models' correlation with the diffusion curves were then checked using the damstart file as a starting envelope for DAMMIN (Figure 4a–c and Table S2). Each DAMAVER envelope appeared as an elongated tube (Figure 4d–f). In parallel, the X-ray structures of MuBV-1 and GaVV-1 were solved using different determination procedures (Table S1). The structure of MuBV-1  $P_{OD}$  was solved by molecular replacement using BoDV-1  $P_{OD}$  as a starting model, whereas GaVV-1  $P_{OD}$  was obtained de novo using Se-Met derivative crystals. For both MuBV-1 and GaVV-1, the asymmetric units contained a tetrameric  $P_{OD}$ , whereas the tetramer for BoDV-1 could be obtained after applying the inherent symmetry operations of the tetragonal space group. Figure 4g–i shows the three biological  $P_{OD}$  (*i.e.*, as tetramers) in the same orientation. The three X-ray structures fit perfectly with the SAXS data. MuBV-1 and GaVV-1  $P_{OD}$  presented similar architectures composed of two  $\alpha$ -helical coiled-coils (the monomers being parallel) linked by a kink. Globally, the only differences concern the relative spatial position of the two coiled-coils, due to the inherent flexibility induced by such a break (Figure S10) and the crystal packing. MuBV-1 and GaVV-1 breaks were also composed of three residues, with a strictly conserved aspartate in the middle (Figure 4j and Figure S9). The Ramachandran analysis showed that all of them fall into the  $\beta$ -area, with neighbouring residues at intermediate positions (Figure S1); this confirms that this specificity is conserved in all Orthobornavirus P.

### 3.4. SAXS Analysis of Full-Length BoDV-1 Phosphoprotein

Having shown that  $P_{OD}$  assembles as a tetramer, we next analysed BoDV-1  $P_{FULL}$  by SAXS in order to provide a complete view of the protein (Table S2). A  $P_{FULL}$  diffusion curve is shown in Figure 5a. Data processing (Figures 5b and S5) indicated that it is elongated for a 201 amino acid-long protein, with a  $D_{max}$  value of  $215 \pm 10$  Å, and Vc determination gives a value of 90 kDa, in accordance with a tetramer in solution, similar to the behaviour of  $P_{OD}$ . The main difference between  $P_{OD}$  and  $P_{FULL}$  became apparent when examining the Kratky plots. Indeed, while a nice bell-shaped (Gaussian) peak was observed for  $P_{OD}$

(Figure S3b), we obtained a curve with a plateau that slowly decays for  $P_{FULL}$  (Figure 5c). These two profiles are characteristic of compact/globular and partially unfolded proteins, respectively, thereby validating our bioinformatic analysis. These data also indicate that the biological unit of BoDV-1 P forms a tetramer in solution, with a central domain responsible for this oligomerisation.

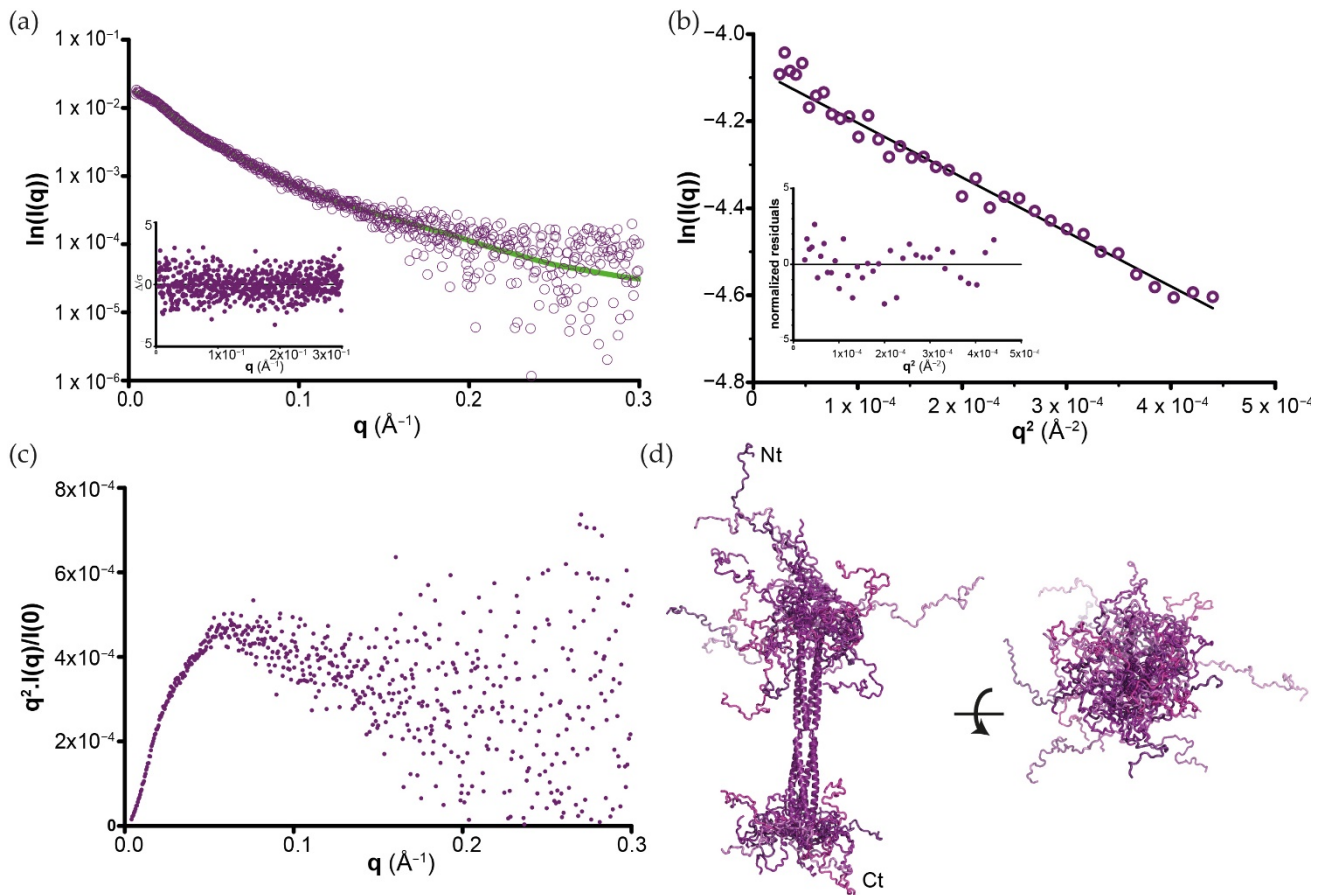


**Figure 5.** Flexibility analysis of BoDV-1 full-length P. (a) Experimental SAXS diffusion curve (deep-purple circles) of  $P_{FULL}$  overlaid with the averaged SAXS curves (green) calculated from the EOM ensemble shown in panel (d). (b) Guinier extrapolation for the determination of the  $R_g$ . The smallest plot corresponds to the normalised residual. (c) Kratky plot showing the partially unfolded propensity of  $P_{FULL}$  samples. (d) Conformational ensemble (6 of 10,000 conformers are shown; these models are perfectly representative of the whole population (Figure S6)) of  $P_{FULL}$  obtained from the modelling procedure based on EOM.  $P_{OD}$  X-ray structure is coloured deep purple, whereas the N- and C-terminal intrinsically disordered regions are coloured with six different shades of purples.

Being partially unfolded, the inherent flexibility of BoDV-1 P complicated the analysis of its structural organisation as a single particle. In order to progress in the complete structural analysis of  $P_{FULL}$ , we used a modelling procedure based on EOM [78] and the  $P_{OD}$  X-ray structure discussed in Section 3.2. A total of 10,000  $C\alpha$  chains corresponding to the missing N- and C-terminal parts were selected to satisfy the SAXS data. Each protein backbone chain was reconstructed from these  $C\alpha$  models [79], and the missing side-chains were finally added with SCWRL4 [80]. Figure 5d shows an ensemble of 6 (out of the 10,000) independent models that fit the SAXS diffusion curves (black line in Figure 5a). This model revealed that despite its rigid central part, BoDV-1 P displays significant flexibility, as illustrated in the figure by the superimposition of the different conformers. However, transitory and/or stable small secondary-structure elements within both N- and C-terminal extremities cannot be excluded in our modelling.

### 3.5. Determination of BoDV-1 P–Host Proximal Interactomics in Living Cells

To gather insights in P<sub>FULL</sub> behaviour in human living cells, we identified its proximity interactors using the BioID technique [91]. BioID uniquely provides information on physical and proximal protein-of-interest partners through the conjugation of biotin on the vicinal free  $\epsilon$ -amine groups of surrounding proteins (within a 10 nm radius [92]). This covalent modification renders possible the thorough solubilisation of all cell compartments using harsh lysis conditions since protein interactions no longer need to be preserved during the purification process. Briefly, we performed BioID using stable and tetracycline-inducible N- and C-terminal BirA\* tagged P<sub>FULL</sub> HEK293 TREx Flp-In cells and purified the biotinylated proteins on streptavidin columns.

We then identified the proximal interactomes by nLC-MS/MS. Following background removal using a set of FlagBirA\* alone samples (localising both in the cytoplasm and the nucleus [93]), we identified a total of 207 high-confidence interactors (Table S3a,b; 147 with FlagBirA\*-P<sub>FULL</sub> and 154 with P<sub>FULL</sub>-BirA\*Flag). As expected, we identified previously reported P<sub>FULL</sub> interactions (*e.g.*, HMGB1 [44] and DNA break repair machineries), but the vast majority of our dataset was novel and links P<sub>FULL</sub> to new mechanisms/complexes. In the set of more than 207 interactors (either nuclear or cytoplasmic), 123 were strictly nuclear, 55 could be in both compartments, and 6 were cytoplasmic (Table S3c). These findings are in agreement with the intrinsic ability of P<sub>FULL</sub> to localise in the nucleus. The relevance of the non-nuclear interactors identified here is subject to caution and could be model-dependent, as discussed hereafter. Word clouds of Gene Ontology enrichment analyses indicated that P could associate with diverse nuclear subcompartments (Figure 6a; *e.g.*, telomeres, nuclear speck, kinetochores) and with factors involved in transcription and DNA repair processes (Figure 6b). Further exploring our data, P<sub>FULL</sub> BioID identified 44 chromatin-associated partners, with 10 and 22 of them being linked to either replication forks or double-strand break repair, respectively (Table S3d; Figure 6c). P<sub>FULL</sub> BioID also detected 52 partners linked to RNA metabolism, including 13 components of the U2-type spliceosomal complex and 6 members involved in mRNA polyadenylation. A comparison between N- and C-terminal BirA\* tagged P<sub>FULL</sub> (Table S3a,e; Figure 6d) revealed that N-terminal BirA\* preferentially identified the HMGB1 and HMGB2 proteins, with HMGB3 being just below the threshold ( $p = 0.014$ ) [94,95], as well as dynactin proteins (DCTN2 and DCTN4). This observation suggests two possibilities: (i) HMGB1/2 and DCTN2/4 proteins interact at the N-terminal region of the BoDV-1 phosphoprotein, with a putative structural “locking” of the twist or of the N-terminal disordered region; (ii) C-terminal tagging of P could hinder these interactions. Conversely, C-terminal tagged P<sub>FULL</sub> preferentially identified two components of the Commander complex (COMMD3 and CCDC22), which are involved in the regulation of NF $\kappa$ B signalling regulation [96]. Similarly, it could indicate an association of these factors with the C-terminal region of P<sub>FULL</sub>, potentially concomitant with an induced structural stiffness, or that the N-terminal tagging impairs their binding or proximity to P<sub>FULL</sub>. Finally, several additional proximal partners were associated with the regulation of innate immune responses (*i.e.*, PQBP1 [97] and its paralog CACTIN [98], HEXIM1 [99], and METTL3 [100]), suggesting a putative function of P in BoDV-1-driven innate immune escape.



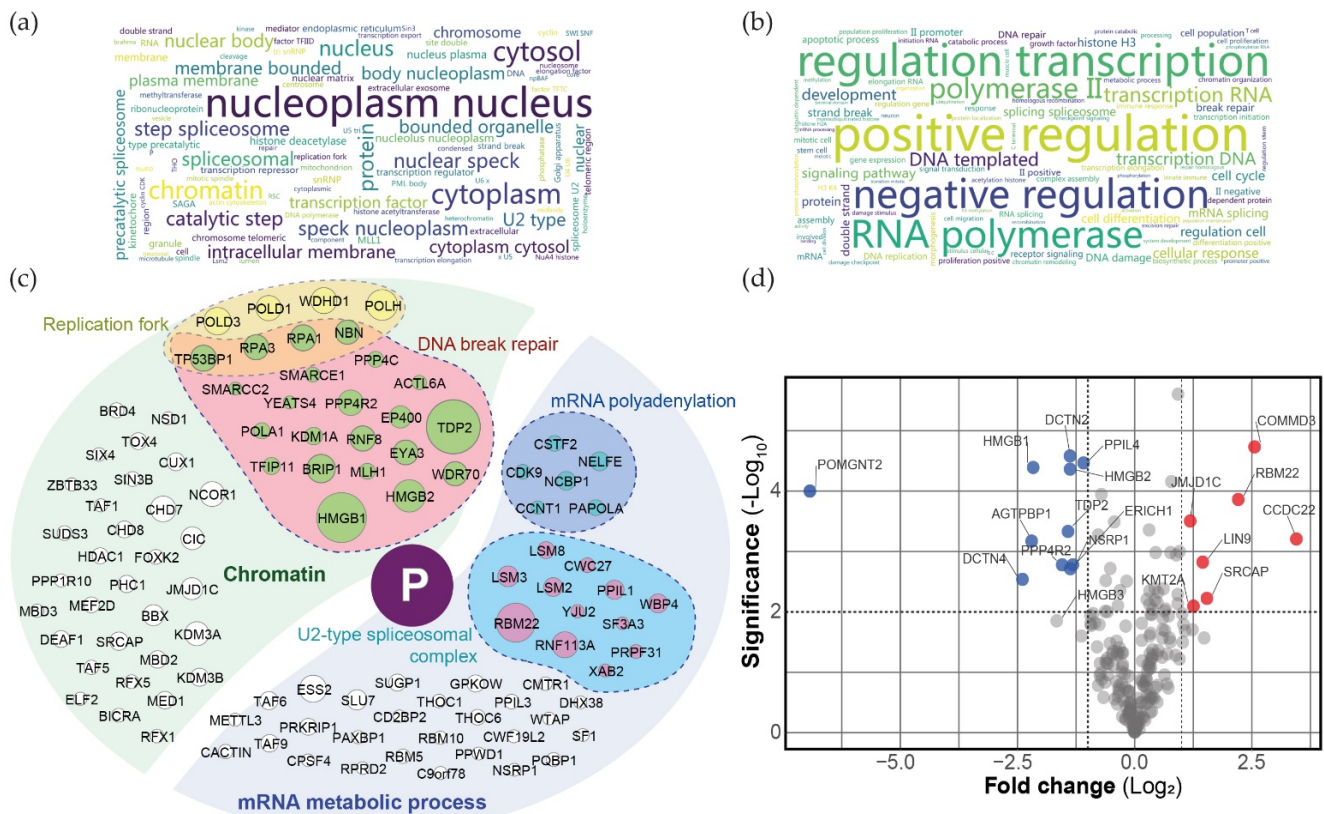


**Figure 6.** Proximal interactomes of P<sub>FULL</sub> in human cells. Word clouds of Gene Ontology enrichment analysis (<https://toppgene.cchmc.org/>; accessed on 1 September 2022) of Cellular Component (a) and Biological Process (b) (assembled on [http://www.bioinformatics.com.cn/plot\\_basic\\_wordcloud\\_11\\_8\\_en](http://www.bioinformatics.com.cn/plot_basic_wordcloud_11_8_en); accessed on 1 September 2022). (c) Illustration of a subset of P<sub>FULL</sub> high-confidence interactors. Proteins are grouped and coloured by selected functions or compartments, as indicated on the diagram; node diameter is proportional to the Log<sub>2</sub> fold change against control. (d) Volcano plot comparing the N- and C-terminal BirA\* tagged BioID data. Blue and red dots represent N- and C-terminal BirA\* tagged preferential partners, respectively ( $p$ -value < 0.01 and Log<sub>2</sub> fold change > 1 between both fusions). Assembled using <https://huygens.science.uva.nl/VolcanoR/>; accessed on 1 September 2022). All data are based on three biological replicates and have been filtered for background against a set of 20 control runs (see Methods and Supplemental Methods for details).

#### 4. Discussion

By interacting with all the proteins of the replication machinery and recruiting many cellular partners, *Mononegavirales* P can be considered as the cornerstone of viral proliferation. Their peculiar architecture consisting of long disordered regions that alternate with structured domains is largely related to all these functions. Our structural findings reveal that orthobornaviral P does not deviate from that model, with an extended central oligomerisation domain that represents half of the size of the protein, surrounded by N- and C-terminal flexible parts. In the past, it was speculated that BoDV-1 P assembled in oligomers, from dimers stabilized by an internal disulfide bridge to tetramers [90,101]. With our data, we confirm that orthobornaviral P forms tetramers in solution, which is in complete agreement with these previous works. There were uncertainties regarding the formation of a trimeric or a tetrameric form in these previous studies, which could be related to the fact that the qualitative analysis of such a protein with disordered propensities was performed using a Superose 12 column [101]. Indeed, disordered and globular proteins are known to be eluted differently from SEC, and the column used at that time was less suited to efficiently discriminate proteins with such small differences in composition. Because of our experimental procedures, in particular during the crystallisation step, we cannot



totally exclude the presence of a disulfide bridge at position 125 for a non-secreted protein [90]. However, the presence of a disulfide bridge at position 125 may not be of primary importance, since C125 is only conserved in mammalian 1 orthobornaviruses P (Figure S8). For the other orthobornaviruses, position 125 (or similar) is occupied by amino acids with different physico-chemical properties (from serine/threonine to leucine/isoleucine). In contrast, D126 is strictly conserved amongst the members of genus *Orthobornavirus*, and our minireplicon assays suggested that it plays an important role in viral replication, without any explanation yet. Future studies examining the role of D126 position in the assembly of the polymerase complex and vSPOT formation will help to better understand the role of this key position.

In *Mononegavirales*, *Bornaviridae* P is the shortest regarding amino acid composition. However, it bears the most elongated oligomerisation domain, although to date, this feature has only been proven in solution, far from the cellular context. Structural data on the *Bornaviridae* L-P complex may be particularly relevant for information about P structure within the replication complex. For instance, P may conserve its elongated structuration, similarly to PIV5, where the tetrameric P<sub>OD</sub> protrudes from the globular RdRp [15]. Alternatively, the twist present in BoDV-1 P<sub>OD</sub> may correspond to a hinge that would favour a structural rearrangement of the cofactor to reach an octopus-like organisation intertwined with L, as seen for RSV [14,102]. However, such a rearrangement would involve the destabilisation of the N- or the C-terminal coiled-coil, which would be energetically consuming. The L binding site for P has been described to be located between residues 135 and 183 [101]. This part of the P<sub>OD</sub> corresponds to the most conserved of the two helical coiled-coils (the sequence conservations of the N- and C-terminal  $\alpha$ -helixes are 30% and 55%, respectively). The C-terminal  $\alpha$ -helix ending at position 162 in our crystal structure, the interaction between L and P could be only mediated by the end of the second  $\alpha$ -helix and a stretch of flexible residues up to 183, without any major rearrangement of the cofactor.

Our results also show that BoDV-1 P presents significant inherent flexibility through its N- and C-terminal parts. This is stressed by the high overlap between the N- and C-terminal BioID tagged P proximal interactomes. Comparing the N- and C-terminal BioID tagged proximal interactomes, we observed that only 45% (94/207) of factors are in common. However, when comparing the relative abundance of the high-confidence interactors, over 90% (189/207) did not show significant differences depending on the tag positioning. This apparent discrepancy is due to stringent filtering used to define high-confidence proximal interactors, and the LFQ comparison between merged hits strongly supports the ability of the BirA\* moiety to conjugate biotin on proteins located in similar places, whether it is positioned at the N- or C-terminal of P. Given that the biotinylation radius of BirA\* has been estimated to be ~10 nm [92], and that that of P<sub>OD</sub> alone is ~14 nm, we hypothesise that the disordered domains remain unstructured in living cells and confer to BirA\* enough freedom to move around the P<sub>OD</sub>, thereby biotinylating similar species. Our analysis of the proximal interactomes confirmed the intrinsic ability of BoDV-1 P to localise at DNA DSBs regions. The interactome analysis particularly pointed out a proximity with sensing factors (TP53BP1) or resolution by repair of the DSB (*i.e.*, NBN, BRIP, PPP4). It also supported its role in recruiting numerous mRNA processing factors, which could serve as complementation factors for vRNA production and maturation in the context of BoDV-1 infection (*e.g.*, mRNA polyadenylation machinery). Considering that BioID identifies proximal partners of the fusion bait protein over 24 h (labelling time roughly equal to one cell cycle in HEK293), our data hence represent a collection of all detectable proteins that were at some point in contact with or in the close vicinity of P<sub>FULL</sub>. Considering that differentiated neurons (the cells targeted by BoDV-1) are postmitotic cells and thus do not enter in mitosis, it is important to stress that our approach must be seen as a discovery step with several limitations to keep in mind. Besides lacking the co-expression of N and L BoDV-1 proteins, which could trigger synergic interactions, labelling over a cell cycle time could explain the presence of a few non-nuclear factors that could interact with BoDV-1 P upon nuclear envelope breakdown (prophase). If this hypothesis

is true, non-nuclear interactors identified here should be considered with caution since P expressed alone would remain strictly nuclear. However, since P is translated in the cytoplasm, these interactions could represent P processing factors before its delivery to the nucleoplasm. In line with the previous remark, we also identified replication fork factors. In view of the tropism of BoDV-1 towards neurons, our data regarding the replication fork components must be considered with caution as well. Given the recruitment of DNA repair machineries on stalled forks during replication stress to repair DNA damage and resume replication ([103] for review), we consider the interactions with the replication fork factor to be model-dependent and not necessarily relevant in an infectious context. However, the frequent occurrence of DNA DSBs and the peculiar centrality of the DNA repair machineries in driving neurons somatic mosaicism and diverse neurodegenerative diseases are well documented (reviewed in [104]). We see our data as a discovery step sketching the ability of BoDV-1 phosphoprotein to interact with ubiquitous DNA repair factors. Moreover, these results may be particularly important in the context of novel findings showing that neuronal DSB responses play key roles in learning and memory [105,106]. For instance, our data could serve as a first step to supervised studies in infected neurons aiming at understanding which of these factors are essential for the positioning of vSPOTs at DNA DSBs. In addition, the identification of proximal partners involved in the regulation of innate immune responses suggests that P could interfere with the host cell's ability to defend against BoDV-1 infection.

Beyond supporting the relevance of our structural model in living cells, our proximal interactomics data represent—to our knowledge—the first published BioID study of any *Mononegavirales* P. Making sense of what is suspected in the field and providing dozens of nuclear ubiquitous factors, this work hence represents an unprecedented wealth of data, which could direct numerous studies aiming at deciphering BoDV-1 P functions in human cells. Repeating such experiments in an infectious context (*i.e.*, complementing with the other BoDV-1 proteins ideally in neurons) would provide information on the cooperation between viral proteins and better resolve the issue of vSPOT composition.

**Supplementary Materials:** The following supporting information can be downloaded at <https://www.mdpi.com/article/10.3390/v14112358/s1>. Experimental procedures: generation of Bio-ID samples; Experimental procedures: BioID data acquisition; Experimental procedures: BioID data analysis; Figure S1: Ramachandran plot of the three P<sub>OD</sub> X-ray structures; Figure S2: Guinier analysis of the P<sub>OD</sub> SAXS analysis; Figure S3: P(R) functions and Krakty plots of the P<sub>OD</sub> SAXS analysis; Figure S4: Orthobornaviral P<sub>OD</sub> SAXS envelopes; Figure S5: P<sub>FULL</sub> P(r) function; Figure S6: Validity of the six P<sub>FULL</sub> models presented in Figure 2d; Figure S7: Detection of BoDV-1 P mutants; Figure S8: Sequence alignment of P from all representative viruses of the genus *Orthobornavirus*; Figure S9: Detailed electron density maps; Figure S10: Orthobornaviral P<sub>OD</sub> flexibility; Figure S11: BoDV-1 P structure prediction by AlphaFold2; Table S1: X-ray data collection and refinement parameters; Table S2: SAXS data collection and scattering-derived parameters; Table S3: BioID data and enrichment analyses. References [108–111] are cited in the supplementary materials

**Author Contributions:** Conceptualization, T.C., M.H., D.G.-D. and E.C.; methodology, N.T., F.C., J.K., K.B., J.-M.B., E.M.N.L., P.L., L.L.F. and T.C.; formal analysis, N.T., J.-M.B., M.H., E.C. and T.C.; writing—original draft preparation, E.C., M.H. and T.C.; writing—review and editing, N.T., D.G.-D., M.H., E.C., E.S., R.W.H.R., K.T. and T.C.; funding acquisition, T.C., D.G.-D., E.C. and M.H. All authors have read and agreed to the published version of the manuscript.

**Funding:** This research was funded by the Agence Nationale de la Recherche (grant Bavarian; ANR-21-CE15-0026) and the Japan Society for the Promotion of Science (Grant-in-Aid for Scientific Research (B): JP21H01199). For this project, F.C. received funding from GRAL (Grenoble Alliance for Integrated Structural and Cell Biology, a program of the Chemistry Biology Health Graduate School of Université Grenoble Alpes (ANR-17-EURE-0003)), K.B. was co-funded by the Ministère de l'Enseignement Supérieur et de la Recherche and the Université de Lille Nord Europe (project MONET), and E.M.N.L. was funded by the Métropole européenne de Lille ("Accueil de Talents" funding scheme).

**Institutional Review Board Statement:** Not applicable.

**Informed Consent Statement:** Not applicable.

**Data Availability Statement:** The X-ray diffraction data are available in the protein databank (<https://www.rcsb.org/>; accessed on 1 September 2022) with the accession numbers 8B8A, 8B8B, and 8B8D for BoDV-1, MuBV-1, and GaVV-1 P<sub>OD</sub>, respectively; the SAXS data can be found in the small-angle scattering biological databank (<https://www.sasbdb.org/>; accessed on 1 September 2022) with the accession numbers SASDQP5, SASDQQ5, SASDQR5, and SASDQS5 for BoDV-1 P<sub>FULL</sub>, BoDV-1, MuBV-1, and GaVV-1 P<sub>OD</sub>, respectively; the mass spectrometry proteomics data have been deposited to the ProteomeXchange Consortium via the PRIDE [107] partner repository with the dataset identifier PDX036750 at <http://www.ebi.ac.uk/pride>; accessed on 1 September 2022 (login: reviewer\_pdx036750@ebi.ac.uk; pw: OXUWT9se).

**Acknowledgments:** We acknowledge Patrice Velicite, Alexandra Mousset, Ambre Valenti, Marwan Hamoudi, and Jean-Pascal Gimeno for technical support, with special thanks to Ada Roy for her involvement. We thank all members of our laboratories for their contributions and helpful discussions. This work used the platforms of the Grenoble Instruct-ERIC centre (ISBG; UAR 3518 CNRS-CEA-UGA-EMBL) within the Grenoble Partnership for Structural Biology (PSB), supported by FRISBI (ANR-10-INBS-0005-02) and GRAL, financed within the University Grenoble Alpes graduate school (Ecoles Universitaires de Recherche) CBH-EUR-GS (ANR-17-EURE-0003). We acknowledge SOLEIL (proposal numbers 20170827 and 20191314) and the ESRF (proposal number MX2285) for provision of synchrotron radiation facilities, and we would like to thank Aurélien Thureau, Pierre Montaville, Andrew Thompson, William Shepard, and Daniele De Sanctis for assistance in using the beamlines SWING, PROXIMA-1, PROXIMA-2A, and ID29, respectively.

**Conflicts of Interest:** The authors declare no conflict of interest.

## References

1. Whelan, S.P.; Barr, J.N.; Wertz, G.W. Transcription and replication of nonsegmented negative-strand RNA viruses. *Curr. Top. Microbiol. Immunol.* **2004**, *283*, 61–119.
2. Kolakofsky, D.; Le Mercier, P.; Nishio, M.; Blackledge, M.; Crepin, T.; Ruigrok, R.W.H. Sendai virus and a unified model of mononegavirus RNA synthesis. *Viruses* **2021**, *13*, 2466. [[CrossRef](#)]
3. Tarbouriech, N.; Curran, J.; Ruigrok, R.W.; Burmeister, W.P. Tetrameric coiled-coil domain of Sendai virus phosphoprotein. *Nat. Struct. Biol.* **2000**, *7*, 777–781.
4. Ding, H.; Green, T.J.; Lu, S.; Luo, M. Crystal structure of the oligomerization domain of the phosphoprotein of vesicular stomatitis virus. *J. Virol.* **2006**, *80*, 2808–2814. [[CrossRef](#)] [[PubMed](#)]
5. Ivanov, I.; Crépin, T.; Jamin, M.; Ruigrok, R.W. Structure of the dimerization domain of the rabies virus phosphoprotein. *J. Virol.* **2010**, *84*, 3707–3710. [[CrossRef](#)]
6. Communie, G.; Crépin, T.; Maurin, D.; Jensen, M.R.; Blackledge, M.; Ruigrok, R.W. Structure of the tetramerization domain of measles virus phosphoprotein. *J. Virol.* **2013**, *87*, 7166–7169. [[CrossRef](#)] [[PubMed](#)]
7. Cox, R.; Green, T.J.; Purushotham, S.; Deivanayagam, C.; Bedwell, G.J.; Prevelige, P.E.; Luo, M. Structural and functional characterization of the mumps virus phosphoprotein. *J. Virol.* **2013**, *87*, 7558–7568. [[CrossRef](#)] [[PubMed](#)]
8. Bruhn, J.F.; Hotard, A.L.; Spiropoulou, C.F.; Lo, M.K.; Saphire, E.O. A conserved basic patch and central kink in the Nipah virus phosphoprotein multimerization domain are essential for polymerase function. *Structure* **2019**, *27*, 660–668 e4. [[CrossRef](#)]
9. Zinzula, L.; Nagy, I.; Orsini, M.; Weyher-Stingl, E.; Bracher, A.; Baumeister, W. Structures of Ebola and Reston virus VP35 oligomerization domains and comparative biophysical characterization in all ebolavirus species. *Structure* **2019**, *27*, 39–54 e6. [[CrossRef](#)]
10. Jensen, M.R.; Yabukarski, F.; Communie, G.; Condamine, E.; Mas, C.; Volchkova, V.; Tarbouriech, N.; Bourhis, J.M.; Volchkov, V.; Blackledge, M.; et al. Structural description of the Nipah virus phosphoprotein and its interaction with STAT1. *Biophys. J.* **2020**, *118*, 2470–2488. [[CrossRef](#)]
11. Wang, Z.X.; Liu, S.B.; Guan, H.; Lu, L.F.; Tu, J.G.; Ouyang, S.; Zhang, Y.A. Structural and functional characterization of the phosphoprotein central domain of spring viremia of carp virus. *J. Virol.* **2020**, *94*. [[CrossRef](#)] [[PubMed](#)]
12. Cardone, C.; Caseau, C.M.; Bardiaux, B.; Thureau, A.; Galloux, M.; Bajorek, M.; Eleouet, J.F.; Litaudon, M.; Bontems, F.; Sizun, C. A structural and dynamic analysis of the partially disordered polymerase-binding domain in RSV phosphoprotein. *Biomolecules* **2021**, *11*, 1225. [[CrossRef](#)] [[PubMed](#)]
13. Gilman, M.S.A.; Liu, C.; Fung, A.; Behera, I.; Jordan, P.; Rigaux, P.; Ysebaert, N.; Tcherniuk, S.; Sourimant, J.; Eleouet, J.F.; et al. Structure of the respiratory syncytial virus polymerase complex. *Cell* **2019**, *179*, 193–204.e14. [[CrossRef](#)] [[PubMed](#)]
14. Cao, D.; Gao, Y.; Roesler, C.; Rice, S.; D’Cunha, P.; Zhuang, L.; Slack, J.; Domke, M.; Antonova, A.; Romanelli, S.; et al. Cryo-EM structure of the respiratory syncytial virus RNA polymerase. *Nat. Commun.* **2020**, *11*, 368. [[CrossRef](#)]

15. Abdella, R.; Aggarwal, M.; Okura, T.; Lamb, R.A.; He, Y. Structure of a paramyxovirus polymerase complex reveals a unique methyltransferase-CTD conformation. *Proc. Natl. Acad. Sci. USA* **2020**, *117*, 4931–4941. [[CrossRef](#)]
16. Jenni, S.; Bloyet, L.M.; Diaz-Avalos, R.; Liang, B.; Whelan, S.P.J.; Grigorieff, N.; Harrison, S.C. Structure of the vesicular stomatitis virus L protein in complex with its phosphoprotein cofactor. *Cell Rep.* **2020**, *30*, 53–60.e5. [[CrossRef](#)]
17. Horwitz, J.A.; Jenni, S.; Harrison, S.C.; Whelan, S.P.J. Structure of a rabies virus polymerase complex from electron cryo-microscopy. *Proc. Natl. Acad. Sci. USA* **2020**, *117*, 2099–2107. [[CrossRef](#)]
18. Pan, J.; Qian, X.; Lattmann, S.; El Sahili, A.; Yeo, T.H.; Jia, H.; Cressey, T.; Ludeke, B.; Noton, S.; Kalocsay, M.; et al. Structure of the human metapneumovirus polymerase phosphoprotein complex. *Nature* **2020**, *577*, 275–279. [[CrossRef](#)]
19. Gould, J.R.; Qiu, S.; Shang, Q.; Ogino, T.; Prevelige, P.E., Jr.; Petit, C.M.; Green, T.J. The connector domain of vesicular stomatitis virus large protein interacts with the viral phosphoprotein. *J. Virol.* **2020**, *94*. [[CrossRef](#)]
20. Green, T.J.; Luo, M. Structure of the vesicular stomatitis virus nucleocapsid in complex with the nucleocapsid-binding domain of the small polymerase cofactor, P. *Proc. Natl. Acad. Sci. USA* **2009**, *106*, 11713–11718. [[CrossRef](#)]
21. Leyrat, C.; Yabukarski, F.; Tarbouriech, N.; Ribeiro, E.A., Jr.; Jensen, M.R.; Blackledge, M.; Ruigrok, R.W.; Jamin, M. Structure of the vesicular stomatitis virus N(0)-P complex. *PLoS Pathog.* **2011**, *7*, e1002248. [[CrossRef](#)] [[PubMed](#)]
22. Yabukarski, F.; Lawrence, P.; Tarbouriech, N.; Bourhis, J.M.; Delaforge, E.; Jensen, M.R.; Ruigrok, R.W.; Blackledge, M.; Volchkov, V.; Jamin, M. Structure of Nipah virus unassembled nucleoprotein in complex with its viral chaperone. *Nat. Struct. Mol. Biol.* **2014**, *21*, 754–759. [[CrossRef](#)] [[PubMed](#)]
23. Guryanov, S.G.; Liljeroos, L.; Kasaragod, P.; Kajander, T.; Butcher, S.J. Crystal structure of the measles virus nucleoprotein core in complex with an N-terminal region of phosphoprotein. *J. Virol.* **2015**, *90*, 2849–2857. [[CrossRef](#)] [[PubMed](#)]
24. Leung, D.W.; Borek, D.; Luthra, P.; Binning, J.M.; Anantpadma, M.; Liu, G.; Harvey, I.B.; Su, Z.; Endlich-Frazier, A.; Pan, J.; et al. An intrinsically disordered peptide from Ebola virus VP35 controls viral RNA synthesis by modulating nucleoprotein-RNA interactions. *Cell Rep.* **2015**, *11*, 376–389. [[CrossRef](#)]
25. Renner, M.; Bertinelli, M.; Leyrat, C.; Paesen, G.C.; Saraiva de Oliveira, L.F.; Huiskonen, J.T.; Grimes, J.M. Nucleocapsid assembly in pneumoviruses is regulated by conformational switching of the N protein. *Elife* **2016**, *5*, e12627. [[CrossRef](#)]
26. Zhu, T.; Song, H.; Peng, R.; Shi, Y.; Qi, J.; Gao, G.F. Crystal structure of the Marburg virus nucleoprotein core domain chaperoned by a VP35 peptide reveals a conserved drug target for Filovirus. *J. Virol.* **2017**, *91*. [[CrossRef](#)]
27. Aggarwal, M.; Leser, G.P.; Kors, C.A.; Lamb, R.A. Structure of the paramyxovirus parainfluenza virus 5 nucleoprotein in complex with an amino-terminal peptide of the phosphoprotein. *J. Virol.* **2018**, *92*. [[CrossRef](#)]
28. Dong, X.; Wang, X.; Xie, M.; Wu, W.; Chen, Z. Structural basis of human parainfluenza virus 3 unassembled nucleoprotein in complex with its viral chaperone. *J. Virol.* **2022**, *96*, e0164821. [[CrossRef](#)]
29. Barik, S.; Banerjee, A.K. Phosphorylation by cellular casein kinase II is essential for transcriptional activity of vesicular stomatitis virus phosphoprotein P. *Proc. Natl. Acad. Sci. USA* **1992**, *89*, 6570–6574. [[CrossRef](#)]
30. Schwemmle, M.; De, B.; Shi, L.; Banerjee, A.; Lipkin, W.I. Borna disease virus P-protein is phosphorylated by protein kinase Cepsilon and casein kinase II. *J. Biol. Chem.* **1997**, *272*, 21818–21823. [[CrossRef](#)]
31. Dupuy, L.C.; Dobson, S.; Bitko, V.; Barik, S. Casein kinase 2-mediated phosphorylation of respiratory syncytial virus phosphoprotein P is essential for the transcription elongation activity of the viral polymerase; phosphorylation by casein kinase 1 occurs mainly at Ser(215) and is without effect. *J. Virol.* **1999**, *73*, 8384–8392. [[CrossRef](#)] [[PubMed](#)]
32. Raux, H.; Flamand, A.; Blondel, D. Interaction of the rabies virus P protein with the LC8 dynein light chain. *J. Virol.* **2000**, *74*, 10212–10216. [[CrossRef](#)] [[PubMed](#)]
33. Sun, M.; Fuentes, S.M.; Timani, K.; Sun, D.; Murphy, C.; Lin, Y.; August, A.; Teng, M.N.; He, B. Akt plays a critical role in replication of nonsegmented negative-stranded RNA viruses. *J. Virol.* **2008**, *82*, 105–114. [[CrossRef](#)] [[PubMed](#)]
34. Kubota, T.; Matsuoka, M.; Chang, T.H.; Bray, M.; Jones, S.; Tashiro, M.; Kato, A.; Ozato, K. Ebolavirus VP35 interacts with the cytoplasmic dynein light chain 8. *J. Virol.* **2009**, *83*, 6952–6956. [[CrossRef](#)] [[PubMed](#)]
35. Leung, D.W.; Ginder, N.D.; Fulton, D.B.; Nix, J.; Basler, C.F.; Honzatko, R.B.; Amarasinghe, G.K. Structure of the Ebola VP35 interferon inhibitory domain. *Proc. Natl. Acad. Sci. USA* **2009**, *106*, 411–416. [[CrossRef](#)]
36. Lahaye, X.; Vidy, A.; Fouquet, B.; Blondel, D. Hsp70 protein positively regulates rabies virus infection. *J. Virol.* **2012**, *86*, 4743–4751. [[CrossRef](#)]
37. Fouquet, B.; Nikolic, J.; Larrous, F.; Bourhy, H.; Wirblich, C.; Lagaudrière-Gesbert, C.; Blondel, D. Focal adhesion kinase is involved in rabies virus infection through its interaction with viral phosphoprotein P. *J. Virol.* **2015**, *89*, 1640–1651. [[CrossRef](#)]
38. Jespersen, N.E.; Leyrat, C.; Gerard, F.C.; Bourhis, J.M.; Blondel, D.; Jamin, M.; Barbar, E. The LC8-RavP ensemble structure convinces a role for LC8 in regulating lyssavirus polymerase functionality. *J. Mol. Biol.* **2019**, *431*, 4959–4977. [[CrossRef](#)]
39. Briggs, K.; Wang, L.; Nagashima, K.; Zengel, J.; Tripp, R.A.; He, B. Regulation of mumps virus replication and transcription by kinase RPS6KB1. *J. Virol.* **2020**, *94*. [[CrossRef](#)]
40. Lim, D.; Shin, H.C.; Choi, J.S.; Kim, S.J.; Ku, B. Crystal structure of human LC8 bound to a peptide from Ebola virus VP35. *J. Microbiol.* **2021**, *59*, 410–416. [[CrossRef](#)]
41. Kuhn, J.H.; Durrwald, R.; Bao, Y.; Briese, T.; Carbone, K.; Clawson, A.N.; deRisi, J.L.; Garten, W.; Jahrling, P.B.; Kolodziejek, J.; et al. Taxonomic reorganization of the family Bornaviridae. *Arch. Virol.* **2015**, *160*, 621–632. [[CrossRef](#)] [[PubMed](#)]



42. Hyndman, T.H.; Shilton, C.M.; Stenglein, M.D.; Wellehan, J.F.X., Jr. Divergent bornaviruses from Australian carpet pythons with neurological disease date the origin of extant Bornaviridae prior to the end-Cretaceous extinction. *PLoS Pathog.* **2018**, *14*, e1006881. [[CrossRef](#)] [[PubMed](#)]
43. Shi, M.; Lin, X.D.; Chen, X.; Tian, J.H.; Chen, L.J.; Li, K.; Wang, W.; Eden, J.S.; Shen, J.J.; Liu, L.; et al. The evolutionary history of vertebrate RNA viruses. *Nature* **2018**, *556*, 197–202. [[CrossRef](#)] [[PubMed](#)]
44. Matsumoto, Y.; Hayashi, Y.; Omori, H.; Honda, T.; Daito, T.; Horie, M.; Ikuta, K.; Fujino, K.; Nakamura, S.; Schneider, U.; et al. Bornavirus closely associates and segregates with host chromosomes to ensure persistent intranuclear infection. *Cell Host Microbe* **2012**, *11*, 492–503. [[CrossRef](#)]
45. Hoffmann, B.; Tappe, D.; Hoper, D.; Herden, C.; Boldt, A.; Mawrin, C.; Niederstrasser, O.; Muller, T.; Jenckel, M.; van der Grinten, E.; et al. A variegated squirrel bornavirus associated with fatal human encephalitis. *N. Engl. J. Med.* **2015**, *373*, 154–162. [[CrossRef](#)] [[PubMed](#)]
46. Korn, K.; Coras, R.; Bobinger, T.; Herzog, S.M.; Lucking, H.; Stohr, R.; Huttner, H.B.; Hartmann, A.; Ensser, A. Fatal encephalitis associated with Borna disease virus 1. *N. Engl. J. Med.* **2018**, *379*, 1375–1377. [[CrossRef](#)]
47. Cadar, D.; Allendorf, V.; Schulze, V.; Ulrich, R.G.; Schlottau, K.; Ebinger, A.; Hoffmann, B.; Hoffmann, D.; Rubbenstroth, D.; Ismer, G.; et al. Introduction and spread of variegated squirrel bornavirus 1 (VSBV-1) between exotic squirrels and spill-over infections to humans in Germany. *Emerg. Microbes Infect.* **2021**, *10*, 602–611. [[CrossRef](#)]
48. Hirai, Y.; Tomonaga, K.; Horie, M. Borna disease virus phosphoprotein triggers the organization of viral inclusion bodies by liquid-liquid phase separation. *Int. J. Biol. Macromol.* **2021**, *192*, 55–63. [[CrossRef](#)]
49. Marty, F.H.; Bettamin, L.; Thouard, A.; Bourgade, K.; Allart, S.; Larrieu, G.; Malnou, C.E.; Gonzalez-Dunia, D.; Suberbielle, E. Borna disease virus docks on neuronal DNA double-strand breaks to replicate and dampens neuronal activity. *iScience* **2022**, *25*, 103621. [[CrossRef](#)]
50. Suberbielle, E.; Stella, A.; Pont, F.; Monnet, C.; Mouton, E.; Lamouroux, L.; Monsarrat, B.; Gonzalez-Dunia, D. Proteomic analysis reveals selective impediment of neuronal remodeling upon Borna disease virus infection. *J. Virol.* **2008**, *82*, 12265–12279. [[CrossRef](#)]
51. Bonnaud, E.M.; Szelechowski, M.; Betourne, A.; Foret, C.; Thouard, A.; Gonzalez-Dunia, D.; Malnou, C.E. Borna disease virus phosphoprotein modulates epigenetic signaling in neurons to control viral replication. *J. Virol.* **2015**, *89*, 5996–6008. [[CrossRef](#)] [[PubMed](#)]
52. Rudolph, M.G.; Kraus, I.; Dickmanns, A.; Eickmann, M.; Garten, W.; Ficner, R. Crystal structure of the borna disease virus nucleoprotein. *Structure* **2003**, *11*, 1219–1226. [[CrossRef](#)] [[PubMed](#)]
53. Neumann, P.; Lieber, D.; Meyer, S.; Dautel, P.; Kerth, A.; Kraus, I.; Garten, W.; Stubbs, M.T. Crystal structure of the Borna disease virus matrix protein (BDV-M) reveals ssRNA binding properties. *Proc. Natl. Acad. Sci. USA* **2009**, *106*, 3710–3715. [[CrossRef](#)] [[PubMed](#)]
54. Kabsch, W. Automatic processing of rotation diffraction data from crystals of initially unknown symmetry and cell constants. *J. Appl. Crystallogr.* **1993**, *26*, 795–800. [[CrossRef](#)]
55. Kabsch, W. Integration, scaling, space-group assignment and post-refinement. *Acta Crystallogr. D Biol. Crystallogr.* **2010**, *66 Pt 2*, 133–144. [[CrossRef](#)]
56. Tickle, I.J.; Flensburg, C.; Keller, P.; Paciorek, W.; Sharff, A.; Vornrhein, C.; Bricogne, G. *STARANISO*; Global Phasing Ltd.: Cambridge, UK, 2017.
57. Vornrhein, C.; Flensburg, C.; Keller, P.; Sharff, A.; Smart, O.; Paciorek, W.; Womack, T.; Bricogne, G. Data processing and analysis with the autoPROC toolbox. *Acta Crystallogr. D Biol. Crystallogr.* **2011**, *67 Pt 4*, 293–302. [[CrossRef](#)]
58. McCoy, A.J.; Grosse-Kunstleve, R.W.; Adams, P.D.; Winn, M.D.; Storoni, L.C.; Read, R.J. Phaser crystallographic software. *J. Appl. Crystallogr.* **2007**, *40 Pt 4*, 658–674. [[CrossRef](#)]
59. Terwilliger, T.C.; Grosse-Kunstleve, R.W.; Afonine, P.V.; Moriarty, N.W.; Zwart, P.H.; Hung, L.W.; Read, R.J.; Adams, P.D. Iterative model building, structure refinement and density modification with the PHENIX AutoBuild wizard. *Acta Crystallogr. D Biol. Crystallogr.* **2008**, *64 Pt 1*, 61–69. [[CrossRef](#)]
60. Adams, P.D.; Afonine, P.V.; Bunkoczi, G.; Chen, V.B.; Davis, I.W.; Echols, N.; Headd, J.J.; Hung, L.W.; Kapral, G.J.; Grosse-Kunstleve, R.W.; et al. PHENIX: A comprehensive Python-based system for macromolecular structure solution. *Acta Crystallogr. D Biol. Crystallogr.* **2010**, *66 Pt 2*, 213–221. [[CrossRef](#)]
61. Emsley, P.; Lohkamp, B.; Scott, W.G.; Cowtan, K. Features and development of Coot. *Acta Crystallogr. D Biol. Crystallogr.* **2010**, *66 Pt 4*, 486–501. [[CrossRef](#)]
62. Cohen, S.X.; Ben Jelloul, M.; Long, F.; Vagin, A.; Knipscheer, P.; Lebbink, J.; Sixma, T.K.; Lamzin, V.S.; Murshudov, G.N.; Perrakis, A. ARP/wARP and molecular replacement: The next generation. *Acta Crystallogr. D Biol. Crystallogr.* **2008**, *64 Pt 1*, 49–60. [[CrossRef](#)]
63. Langer, G.; Cohen, S.X.; Lamzin, V.S.; Perrakis, A. Automated macromolecular model building for X-ray crystallography using ARP/wARP version 7. *Nat. Protoc.* **2008**, *3*, 1171–1179. [[CrossRef](#)] [[PubMed](#)]
64. Murshudov, G.N. Refinement of macromolecular structures by the maximum-likelihood method. *Acta Crystallogr. D Biol. Crystallogr.* **1997**, *53 Pt 3*, 240–255. [[CrossRef](#)]
65. Sheldrick, G.M. A short history of SHELX. *Acta Crystallogr. A* **2008**, *64 Pt 1*, 112–122. [[CrossRef](#)]



66. Cowtan, K. Recent developments in classical density modification. *Acta Crystallogr. D Biol. Crystallogr.* **2010**, *66 Pt 4*, 470–478. [[CrossRef](#)]
67. Jumper, J.; Evans, R.; Pritzel, A.; Green, T.; Figurnov, M.; Ronneberger, O.; Tunyasuvunakool, K.; Bates, R.; Zidek, A.; Potapenko, A.; et al. Highly accurate protein structure prediction with AlphaFold. *Nature* **2021**, *596*, 583–589. [[CrossRef](#)]
68. Schrodinger, LLC. *The PyMOL Molecular Graphics System*, Version 1.8; Schrödinger, Inc.: New York, NY, USA, 2015.
69. Thureau, A.; Roblin, P.; Perez, J. BioSAXS on the SWING beamline at Synchrotron SOLEIL. *J. Appl. Crystallogr.* **2021**, *54*, 1698–1710. [[CrossRef](#)]
70. Manalastas-Cantos, K.; Konarev, P.V.; Hajizadeh, N.R.; Kikhney, A.G.; Petoukhov, M.V.; Molodenskiy, D.S.; Panjkovich, A.; Mertens, H.D.T.; Gruzinov, A.; Borges, C.; et al. ATSAS 3.0: Expanded functionality and new tools for small-angle scattering data analysis. *J. Appl. Crystallogr.* **2021**, *54*, 343–355. [[CrossRef](#)] [[PubMed](#)]
71. Hopkins, J.B.; Gillilan, R.E.; Skou, S. BioXTAS RAW: Improvements to a free open-source program for small-angle X-ray scattering data reduction and analysis. *J. Appl. Crystallogr.* **2017**, *50*, 1545–1553. [[CrossRef](#)] [[PubMed](#)]
72. Svergun, D. Determination of the regularization parameter in indirect-transform methods using perceptual criteria. *J. Appl. Crystallogr.* **1992**, *25*, 495–503. [[CrossRef](#)]
73. Hansen, S. Bayesian estimation of hyperparameters for indirect Fourier transformation in small-angle scattering. *J. Appl. Crystallogr.* **2000**, *33*, 1415–1421. [[CrossRef](#)]
74. Rambo, R.P.; Tainer, J.A. Accurate assessment of mass, models and resolution by small-angle scattering. *Nature* **2013**, *496*, 477–481. [[CrossRef](#)] [[PubMed](#)]
75. Franke, D.; Svergun, D.I. DAMMIF, a program for rapid *ab initio* shape determination in small-angle scattering. *J. Appl. Crystallogr.* **2009**, *42 Pt 2*, 342–346. [[CrossRef](#)]
76. Volkov, V.V.; Svergun, D.I. Uniqueness of *ab initio* shape determination in small-angle scattering. *J. Appl. Crystallogr.* **2003**, *36*, 860–864. [[CrossRef](#)]
77. Svergun, D.I. Restoring low resolution structure of biological macromolecules from solution scattering using simulated annealing. *Biophys. J.* **1999**, *76*, 2879–2886. [[CrossRef](#)]
78. Tria, G.; Mertens, H.D.; Kachala, M.; Svergun, D.I. Advanced ensemble modelling of flexible macromolecules using X-ray solution scattering. *IUCr* **2015**, *2 Pt 2*, 207–217. [[CrossRef](#)]
79. Moore, B.L.; Kelley, L.A.; Barber, J.; Murray, J.W.; MacDonald, J.T. High-quality protein backbone reconstruction from alpha carbons using Gaussian mixture models. *J. Comput. Chem.* **2013**, *34*, 1881–1889. [[CrossRef](#)]
80. Krivov, G.G.; Shapovalov, M.V.; Dunbrack, R.L., Jr. Improved prediction of protein side-chain conformations with SCWRL4. *Proteins* **2009**, *77*, 778–795. [[CrossRef](#)]
81. Kanda, T.; Horie, M.; Komatsu, Y.; Tomonaga, K. The Borna disease virus 2 (BoDV-2) nucleoprotein is a conspecific protein that enhances BoDV-1 RNA-dependent RNA polymerase activity. *J. Virol.* **2021**, *95*, e0093621. [[CrossRef](#)] [[PubMed](#)]
82. Reuter, A.; Horie, M.; Höper, D.; Ohnemus, A.; Narr, A.; Rinder, M.; Beer, M.; Staeheli, P.; Rubbenstroth, D. Synergistic antiviral activity of ribavirin and interferon- $\alpha$  against parrot bornaviruses in avian cells. *J. Gen. Virol.* **2016**, *97*, 2096–2103. [[CrossRef](#)]
83. Tu, Y.X.I.; Sydor, A.M.; Coyaud, E.; Laurent, E.M.N.; Dyer, D.; Mellouk, N.; St-Germain, J.; Vernon, R.M.; Forman-Kay, J.D.; Li, T.; et al. Global proximity interactome of the human macroautophagy pathway. *Autophagy* **2022**, *18*, 1174–1186. [[CrossRef](#)] [[PubMed](#)]
84. Gerard, F.C.; Ribeiro Ede, A., Jr.; Leyrat, C.; Ivanov, I.; Blondel, D.; Longhi, S.; Ruigrok, R.W.; Jamin, M. Modular organization of rabies virus phosphoprotein. *J. Mol. Biol.* **2009**, *388*, 978–996. [[CrossRef](#)] [[PubMed](#)]
85. Crick, F.H.C. The Fourier transform of a coiled-coil. *Acta Crystallogr.* **1953**, *6*, 685–689. [[CrossRef](#)]
86. Crick, F.H.C. The packing of  $\alpha$ -helices: Simple coiled-coils. *Acta Crystallogr.* **1953**, *6*, 689–697. [[CrossRef](#)]
87. Grigoryan, G.; Degrado, W.F. Probing designability via a generalized model of helical bundle geometry. *J. Mol. Biol.* **2011**, *405*, 1079–1100. [[CrossRef](#)]
88. Strelkov, S.V.; Burkhard, P. Analysis of alpha-helical coiled-coils with the program TWISTER reveals a structural mechanism for stutter compensation. *J. Struct. Biol.* **2002**, *137*, 54–64. [[CrossRef](#)]
89. Hartmann, M.D.; Mendler, C.T.; Bassler, J.; Karamichali, I.; Ridderbusch, O.; Lupas, A.N.; Hernandez Alvarez, B. alpha/beta coiled-coils. *Elife* **2016**, *5*, 351–358. [[CrossRef](#)]
90. Kliche, S.; Stitz, L.; Mangalam, H.; Shi, L.; Binz, T.; Niemann, H.; Briese, T.; Lipkin, W.I. Characterization of the Borna disease virus phosphoprotein, p23. *J. Virol.* **1996**, *70*, 8133–8137. [[CrossRef](#)]
91. Roux, K.J.; Kim, D.I.; Raida, M.; Burke, B. A promiscuous biotin ligase fusion protein identifies proximal and interacting proteins in mammalian cells. *J. Cell Biol.* **2012**, *196*, 801–810. [[CrossRef](#)]
92. Kim, D.I.; Birendra, K.C.; Zhu, W.; Motamedchaboki, K.; Doye, V.; Roux, K.J. Probing nuclear pore complex architecture with proximity-dependent biotinylation. *Proc. Natl. Acad. Sci. USA* **2014**, *111*, E2453–E2461. [[CrossRef](#)]
93. Mehus, A.A.; Anderson, R.H.; Roux, K.J. BioID Identification of Lamin-Associated Proteins. *Methods Enzymol.* **2016**, *569*, 3–22.
94. Kamitani, W.; Shoya, Y.; Kobayashi, T.; Watanabe, M.; Lee, B.J.; Zhang, G.; Tomonaga, K.; Ikuta, K. Borna disease virus phosphoprotein binds a neurite outgrowth factor, amphoterin/HMG-1. *J. Virol.* **2001**, *75*, 8742–8751. [[CrossRef](#)] [[PubMed](#)]
95. Zhang, G.; Kobayashi, T.; Kamitani, W.; Komoto, S.; Yamashita, M.; Baba, S.; Yanai, H.; Ikuta, K.; Tomonaga, K. Borna disease virus phosphoprotein represses p53-mediated transcriptional activity by interference with HMGB1. *J. Virol.* **2003**, *77*, 12243–12251. [[CrossRef](#)] [[PubMed](#)]

96. Starokadomskyy, P.; Gluck, N.; Li, H.; Chen, B.; Wallis, M.; Maine, G.N.; Mao, X.; Zaidi, I.W.; Hein, M.Y.; McDonald, F.J.; et al. CCDC22 deficiency in humans blunts activation of proinflammatory NF-kappaB signaling. *J. Clin. Investig.* **2013**, *123*, 2244–2256. [[CrossRef](#)] [[PubMed](#)]
97. Yoh, S.M.; Schneider, M.; Seifried, J.; Soonthornvacharin, S.; Akleh, R.E.; Olivieri, K.C.; De Jesus, P.D.; Ruan, C.; de Castro, E.; Ruiz, P.A.; et al. PQBP1 Is a proximal sensor of the cGAS-dependent innate response to HIV-1. *Cell* **2015**, *161*, 1293–1305. [[CrossRef](#)]
98. Atzei, P.; Gargan, S.; Curran, N.; Moynagh, P.N. Cactin targets the MHC class III protein IkappaB-like (IkappaBL) and inhibits NF-kappaB and interferon-regulatory factor signaling pathways. *J. Biol. Chem.* **2010**, *285*, 36804–36817. [[CrossRef](#)]
99. Morchikh, M.; Cribier, A.; Raffel, R.; Amraoui, S.; Cau, J.; Severac, D.; Dubois, E.; Schwartz, O.; Bennasser, Y.; Benkirane, M. HEXIM1 and NEAT1 long non-coding RNA form a multi-subunit complex that regulates DNA-mediated innate immune response. *Mol. Cell* **2017**, *67*, 387–399.e5. [[CrossRef](#)] [[PubMed](#)]
100. Qiu, W.; Zhang, Q.; Zhang, R.; Lu, Y.; Wang, X.; Tian, H.; Yang, Y.; Gu, Z.; Gao, Y.; Yang, X.; et al. N(6)-methyladenosine RNA modification suppresses antiviral innate sensing pathways via reshaping double-stranded RNA. *Nat. Commun.* **2021**, *12*, 1582. [[CrossRef](#)] [[PubMed](#)]
101. Schneider, U.; Blechschmidt, K.; Schwemmler, M.; Staeheli, P. Overlap of interaction domains indicates a central role of the P protein in assembly and regulation of the Borna disease virus polymerase complex. *J. Biol. Chem.* **2004**, *279*, 55290–55296. [[CrossRef](#)] [[PubMed](#)]
102. Gilman, M.S.A.; Furmanova-Hollenstein, P.; Pascual, G.; B van't Wout, A.; Langedijk, J.P.M.; McLellan, J.S. Transient opening of trimeric prefusion RSV F proteins. *Nat. Commun.* **2019**, *10*, 2105. [[CrossRef](#)]
103. Cortez, D. Replication-Coupled DNA Repair. *Mol. Cell* **2019**, *74*, 866–876. [[CrossRef](#)] [[PubMed](#)]
104. Qing, X.; Zhang, G.; Wang, Z.Q. DNA damage response in neurodevelopment and neuromaintenance. *FEBS J.* **2022**. [[CrossRef](#)] [[PubMed](#)]
105. Suberbielle, E.; Sanchez, P.E.; Kravitz, A.V.; Wang, X.; Ho, K.; Eilertson, K.; Devidze, N.; Kreitzer, A.C.; Mucke, L. Physiologic brain activity causes DNA double-strand breaks in neurons, with exacerbation by amyloid-beta. *Nat. Neurosci.* **2013**, *16*, 613–621. [[CrossRef](#)] [[PubMed](#)]
106. Suberbielle, E.; Djukic, B.; Evans, M.; Kim, D.H.; Taneja, P.; Wang, X.; Finucane, M.; Knox, J.; Ho, K.; Devidze, N.; et al. DNA repair factor BRCA1 depletion occurs in Alzheimer brains and impairs cognitive function in mice. *Nat. Commun.* **2015**, *6*, 8897. [[CrossRef](#)]
107. Perez-Riverol, Y.; Bai, J.; Bandla, C.; Garcia-Seisdedos, D.; Hewapathirana, S.; Kamatchinathan, S.; Kundu, D.J.; Prakash, A.; Frericks-Zipper, A.; Eisenacher, M.; et al. The PRIDE database resources in 2022: A hub for mass spectrometry-based proteomics evidences. *Nucleic Acids Res.* **2022**, *50*, D543–D552. [[CrossRef](#)]
108. Goedhart, J.; Luijsterburg, M.S. VolcaNoseR is a web app for creating, exploring, labeling and sharing volcano plots. *Sci. Rep.* **2020**, *10*, 20560. [[CrossRef](#)] [[PubMed](#)]
109. Williams, C.J.; Headd, J.J.; Moriarty, N.W.; Prisant, M.G.; Videau, L.L.; Deis, L.N.; Verma, V.; Keedy, D.A.; Hintze, B.J.; Chen, V.B.; et al. MolProbity: More and better reference data for improved all-atom structure validation. *Protein Sci.* **2018**, *27*, 293–315. [[CrossRef](#)]
110. Larkin, M.A.; Blackshields, G.; Brown, N.P.; Chenna, R.; McGettigan, P.A.; McWilliam, H.; Valentin, F.; Wallace, I.M.; Wilm, A.; Lopez, R.; et al. Clustal W and Clustal X version 2.0. *Bioinformatics* **2007**, *23*, 2947–2948. [[CrossRef](#)]
111. Gouet, P.; Courcelle, E.; Stuart, D.I.; Metz, F. ESPript: Analysis of multiple sequence alignments in PostScript. *Bioinformatics* **1999**, *15*, 305–308. [[CrossRef](#)]